InSAR-derived horizontal velocities in a global reference frame

Milan Lazecky[1] and Andrew Hooper[2]

[1]University of Leeds
[2]University of Leeds, COMET

November 24, 2022

Abstract

Interferometric Synthetic Aperture Radar (InSAR) is used to measure deformation rates over whole continents to constrain tectonic processes. The resulting velocity measurements are only relative, due to unknown integer ambiguities introduced during propagation of the signal through the atmosphere. However, these ambiguities mostly cancel when using spectral diversity to estimate along-track motion, allowing measurements to be made with respect to a global reference frame. Here, we calculate along-track velocities for a partial global dataset of Sentinel-1 acquisitions and find good agreement with ITRF2014 model values. We include corrections for solid-earth tides and gradients of ionospheric total electron content. By combining data from ascending and descending orbits we are able to estimate north and east velocities with average precision of 4 and 20 mm/year, respectively. Although we have calculated these over large 250x250 km areas, such measurements can also be made at much higher resolution, albeit with lower accuracy. These "absolute" measurements can be particularly useful for global velocity and strain rate estimation, where GNSS measurements are sparse.

InSAR-derived horizontal velocities in a global reference frame

M. Lazecký[1], and A. J. Hooper[1]

[1]COMET, School of Earth and Environment, University of Leeds, LS2 9JT Leeds, United Kingdom

Key Points:

- We can use Sentinel-1 InSAR to measure along-track velocities over wide areas in a global reference frame
- Horizontal velocity vectors can then be estimated, which generally agree with the ITRF2014 plate motion model
- The updated Sentinel-1 precise orbits introduced in mid-2020 improve the precision and induce a single offset

Corresponding author: Milan Lazecký, `M.Lazecky@leeds.ac.uk`

Abstract

Interferometric Synthetic Aperture Radar (InSAR) is used to measure deformation rates over whole continents to constrain tectonic processes. The resulting velocity measurements are only relative, due to unknown integer ambiguities introduced during propagation of the signal through the atmosphere. However, these ambiguities mostly cancel when using spectral diversity to estimate along-track motion, allowing measurements to be made with respect to a global reference frame. Here, we calculate along-track velocities for a partial global dataset of Sentinel-1 acquisitions and find good agreement with ITRF2014 model values. We include corrections for solid-earth tides and gradients of ionospheric total electron content. By combining data from ascending and descending orbits we are able to estimate north and east velocities with average precision of 4 and 20 mm/year, respectively. Although we have calculated these over large 250x250 km areas, such measurements can also be made at much higher resolution, albeit with lower accuracy. These "absolute" measurements can be particularly useful for global velocity and strain rate estimation, where GNSS measurements are sparse.

Plain Language Summary

It is possible to use repeated radar measurements from satellites to measure movement of the ground towards or away from the satellite very accurately. These measurements do not tell us the absolute movement, however, but rather the difference in movement between any two parts of the ground captured in the same radar image. Using a related technique, we measure horizontal movement of the ground in the flight direction of the satellite, and these are absolute measurements, in global reference frame. By combing measurements from different flight directions, we can estimate the horizontal movement of the ground in any direction. Our estimates largely match what we expect from plate tectonics. These measurements can be useful for large scale mapping of ground movement, which can be used to better understand how the Earth deforms and how earthquake hazard varies across the globe.

1 Introduction

With the Copernicus Sentinel-1 Synthetic Aperture Radar (SAR) satellites, the geoscience community acquired a unique tool for making precise measurements of tectonic motions. The Centre for Observation and Modelling of Earthquakes, Volcanoes and Tectonics (COMET) LiCSAR system (Lazecký et al., 2020) routinely generates Sentinel-1 differential interferograms over tectonic and volcanic areas, and carries out interferometric (InSAR) time series analyses to measure surface deformation in the satellite line-of-sight direction. The InSAR measurements can be used to derive vertical and horizontal motion components, but the line-of-sight sensitivity is very low for the N-S motion component, which is typically estimated using available GNSS data (Weiss et al., 2020). It is possible to estimate along-track displacements, which are sensitive to N-S motions, by exploiting spectral diversity in the azimuth direction (Bechor & Zebker, 2006), although the precision is poor. However, the Terrain Observation with Progressive Scan (TOPS) acquisition mode of Sentinel-1, which is the standard mode over land, provides much greater spectral diversity in burst overlap regions, allowing estimation with a precision of around 1 mm within whole overlaps (Grandin et al., 2016). Time series approaches have also been developed to estimate along-track velocities in the burst overlap regions (Hooper et al., 2020; Li et al., 2021). These studies treat the along-track velocities as relative measurements, but here we explore how accurately we can measure them in a global reference frame, as the along-track measurements are with respect to reference satellite positions, localised within the Earth-centered Earth-fixed no-net-rotation framework of the ITRF2014. We estimate the velocities in relatively large blocks containing many burst overlaps, in order to observe large-scale tectonic motion and characterise some of the error sources, such as the solid-earth tides and ionosphere.

2 Estimating along-track displacements

We extract the Level-1 single-look complex (SLC) data of the standard Sentinel-1 Interferometric Wide Swath burst units, and merge those bursts into larger spatial frames that we have defined. One typical frame consists of 13 bursts in each of the three swaths and covers an area of approx. 250x250 km. We perform a standard procedure to coregister the SLC data for each acquisition towards a reference epoch (Lazecký et al., 2020). During this process, values of the mean subpixel shift in the azimuth direction, Δa_{px}, are estimated.

In detail, we use the Copernicus Sentinel-1 Precise Orbit Determination ephemerides to resample each SLC into the geometry of the reference epoch, considering topography with respect to the WGS-84 reference ellipsoid (Lazecký et al., 2020). We then run several iterations of intensity cross correlation to estimate a refined sub-pixel shift in both slant range (across-track), $\Delta r_{ICC,px}$, and azimuth (along-track), $\Delta a_{ICC,px}$, directions, with a precision of around 0.01 pixels. Next, we resample the SLC to an intermediate product and iteratively estimate a further refined azimuth coregistration offset $\Delta a_{SD,px}$ using spectral diversity of burst overlaps (De Zan & Monti Guarnieri, 2006). Burst overlap areas are imaged with multiple lines of sight, and differencing interferograms formed for each line-of-sight cancels the across-track displacement, and leads to an estimate of the along-track offset with a precision of around 0.0005 pixels. To ensure coherence, this offset is estimated between pairs of acquisitions close in time that were previously resampled to the reference epoch, thus already shifted by their along-track offset (Lazecký et al., 2020). The spectral diversity phase is related to azimuth pixel shift by (Yagüe-Martínez et al., 2016)

$$\Delta a_{SD,px} = \frac{\Delta\phi_{SD}\, PRF}{2\pi\Delta f_{DC}}, \tag{1}$$

where $PRF = 486.486$ Hz is the pulse repetition frequency (azimuth sampling rate) of the Sentinel-1 system, and Δf_{DC} is the Doppler centroid frequency difference in the burst overlap area.

We sum the frame averages of the subpixel offsets into the final frame-wise Δa_{px} values, to provide offsets with respect to the reference frame of the orbit ephemerides, which is the International Terrestrial Reference System in its ITRF2014 realisation since 2017-02-16, *i.e.*, since version 1.3 of the precise orbit generating system (Peter et al., 2021). We also extract other relevant information on a frame basis, such as average ground footprint heading angle, α, pixel resolution in the azimuth direction, r_{azi}, average incidence angle within the frame, Θ_{inc}, and an average value Δf_{DC} of Doppler frequency difference between burst overlaps, calculated as in (Grandin et al., 2016). We then use r_{azi} in Eq. 2 to convert the frame-wise azimuth pixel offset shift Δa_{px} to the frame-wise measurement Δa [mm] that directly relates to an along-track (azimuth direction) ground displacement.

$$\Delta a = \Delta a_{px}\, r_{azi} = (\Delta a_{ICC,px} + \Delta a_{SD,px})\, r_{azi}. \tag{2}$$

In total, we selected 107,476 Δa values from 1,063 LiCSAR frames, that have a minimum count of 30 Δa values per frame. As the LiCSAR processing currently concentrates on the Alpine-Himalayan orogenic belt (AHB), we provide outputs of our analyses in both full global dataset and the AHB subset, defined by a bounding box of 25°W−110°W and 25°N−45°N. Acquisitions after 2020-07-30 used orbit ephemerides generated by version 1.7 of the orbit determination system, introducing a major correction (Peter et al., 2021).

3 Contributions to the azimuth shifts

Several factors contribute to offsets measured in the along track direction:

$$\Delta a = \Delta a_{tecton} + \Delta a_{tide} + \Delta a_{iono} + \varepsilon, \tag{3}$$

where Δa_{tecton} is the motion due to tectonic displacement between acquisitions, Δa_{tide} is displacement due to the difference in the solid-earth tides between acquisitions, Δa_{iono}

is due to the change in the along-track gradient of total electron content (TEC) between acquisitions, and ε is any residual due to orbit inaccuracies and noise.

As our aim is to isolate Δa_{tecton}, we estimate and subtract values for Δa_{tide} and Δa_{iono}. For Δa_{tide} we use a solid-earth tide model (Petit & Luzum, 2013) and calculate motion in the along-track direction for the centre coordinates of each frame from the tidal components d_E, d_N in the east and north, respectively, using Eq. 4.

$$\Delta a_{tide} = d_E \sin(\alpha) + d_N \cos(\alpha). \tag{4}$$

To estimate Δa_{iono}, we apply the IRI2016 model (Bilitza et al., 2017), using the inverse of the approach for estimating the ionospheric influence on spectral diversity values (Gomba et al., 2016). For each acquisition, we use the IRI2016 model to estimate the TEC between the satellite and the ground in the centre of the image for a hypothetical forward-looking (A) and backward-looking (B) burst, respectively, *i.e.* in a geometry similar to the solution of (Liang et al., 2019). We calculate the location of the respective points A, B, following the azimuth direction footprint below the ionosphere piercing point located in the line-of-sight at the height of the ionospheric F2 layer peak, H_{iono}, which is given by IRI2016. We estimate the incidence angle below the ionosphere piercing point Θ_{IPP} according to the ionospheric single layer model (Ya'acob et al., 2010) and use it to convert modeled TEC_v column to the slant (line-of-sight) direction, TEC_s, as:

$$TEC_s = \frac{TEC_v}{\sqrt{1 - \sin\Theta_{IPP}{}^2}} = \frac{TEC_v}{\sqrt{1 - (\frac{R\sin\Theta}{R+H_{iono}})^2}}, \tag{5}$$

where R is the radius of the Earth.

The TEC_s difference approximately corresponds to the ionospheric influence of the SAR carrier wave of frequency, f_0, modulated by the Doppler effect from the satellite motion and the beam steering during the TOPS acquisition mode in the frequency range $f_A, f_B = f_0 \pm 0.5\Delta f_{DC}$ at the burst edges (Grandin et al., 2016). The phase advance due to propagation through ionosphere is (Gomba et al., 2016):

$$\phi_{iono} = \frac{4\pi\, K}{c\, f} TEC, \tag{6}$$

where $K = 40.308193\,\frac{m^3}{s^2}$ is a constant for which we assume a commonly applied value (Hoque & Jakowski, 2012) and c is the speed of light in vacuum. From Equations **??**, 1, 2, 6, we can derive Δa_{iono} towards the frame reference epoch as

$$\Delta a_{iono} = \frac{2\, PRF\, K}{c\, \Delta f_{DC}} \left(\frac{\Delta TEC_s(A)}{f_A} - \frac{\Delta TEC_s(B)}{f_B} \right) r_{azi}, \tag{7}$$

where ΔTEC_s is the difference between the TEC_s estimate for each acquisition and the reference epoch, and $\Delta f_{DC} = f_A - f_B$, which varies significantly between swaths. An influence of the absolute magnitude of ΔTEC is not expected on the azimuth shift (Gomba et al., 2016; Fattahi, Simons, & Agram, 2017).

We expect the tide model to be sufficiently precise for this analysis, although updated tide models exist, which also consider ocean tide loading or polar motion (Ducarme & Schüller, 2018; Martens et al., 2019). For the ionosphere, the IRI2016 model is a set of equations using several parameters calibrated based on data available at relatively low frequency (months), and IRI2016 estimates are considered relatively accurate for investigating monthly averages. We expect this model to be sufficient for reduction of seasonal fluctuations of Δa caused by ionospheric influence but not for a precise estimate per each Δa sample.

Figure 1 demonstrates the influence of the implemented corrections applied to the original Δa values. The time series are based on median-corrected Δa values, filtered by a rolling median using 10 samples, and plotted by a colour gradient representing distance of each frame centre from the Equator.

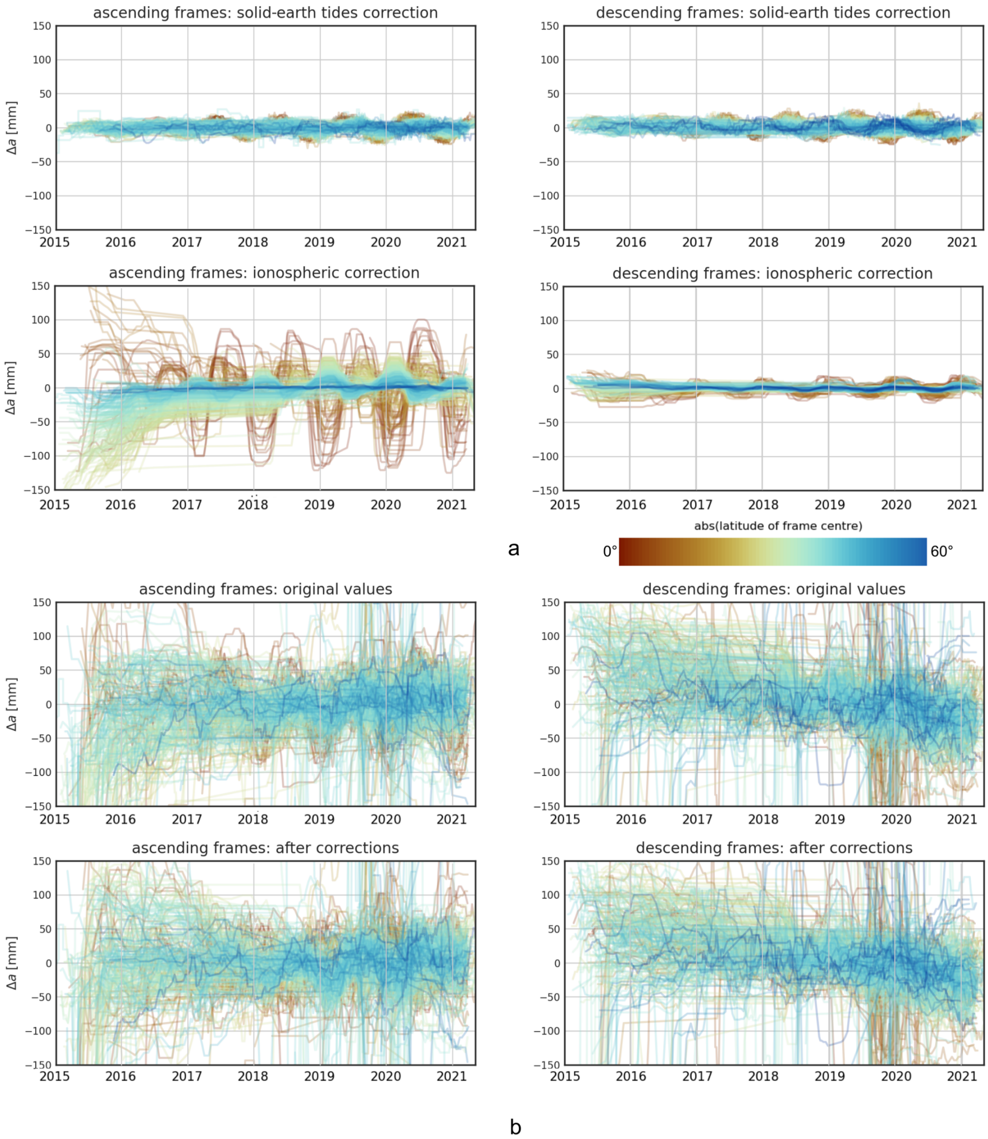

Figure 1. Effect of solid-earth tides and ionospheric corrections on time series of Δa values for, left, ascending and, right, descending frames; colour gradient is based on distance from the Equator: a) time series of modeled Δa corrections at the same scale; b) Δa values before and after corrections; Δa values are after correction for updated orbits (see Section 4).

4 Effect of updated orbit ephemerides

The orbit emphemerides products of Sentinel-1 changed on 30th July 2020 to version 1.7, incorporating a correction of the on-board GPS antenna reference point position, as identified by (Peter et al., 2020). This correction implied a 3-D position change of approx. 6 cm which led to a decrease in the the root mean square error (RMSE) of the 3-D position of the satellites to below 1 cm (Peter et al., 2021). The antenna reference point is shifted by 39 mm in the along-track direction of the satellite, see Tables 3-1 and 3-2 in Fernández et al. (2019). We investigate the effect of the reference point shift on the azimuth shift, by comparing acquisitions processed using the old and new orbits. Additionally, as the updated orbits should improve precision of satellite positioning, we explore whether there is a decrease in error of Δa measurements. For the analyses in this section, we use Δa values corrected for both solid-earth tides and ionosphere.

4.1 Estimation of offset due to updated orbits

We expect the use of updated orbits would to cause a constant offset in the linear model of along-track velocities. We split the dataset of Δa values by the date of orbits update, 2020-07-30, and select only values after 2016-07-30 to lower the impact of residual ionosphere. We then estimate preliminary model parameters m of linear velocity v', intercept c, and offset due to orbit change $\delta\Delta a$ by applying least squares inversion to

$$
\begin{aligned}
d &= A\,m \\
\begin{bmatrix} \Delta a_1 \\ \vdots \\ \Delta a_n \end{bmatrix} &= \begin{bmatrix} \Delta t_1 & 1 & 0 \\ \vdots & \vdots & \vdots \\ \Delta t_n & 1 & 1 \end{bmatrix} \begin{bmatrix} v' \\ c \\ \delta\Delta a \end{bmatrix},
\end{aligned}
\tag{8}
$$

where Δt is the acquisition time in years since 2016-07-30, and the final columns is 1 for acquisition times after the orbits change date. After performing the inversion per frame, we remove outliers above 3 RMSE from median, and after re-estimating model parameters, we drop frames having RMSE above 120 mm. The final mean offset value is then estimated from 484 frames as -39.9 ± 3.7 mm at 2-sigma error, which agrees with the expected shift due to orbit change, of -39 mm, within error. We plot distribution of the estimated offsets per orbital tracks in histograms in Fig. 2a.

4.2 Impact of updated orbits on Δa precision

We extract one-year subsets from the data set for both before and after the orbit change (*pre* and *post* subsets), and ensure there is an equal number of samples per subset. We then calculate RMSE values σ_{pre}, σ_{post} per subset, and observe median improvement in precision of Δa after the orbit update as $\overline{\Delta RMSE} = -4.7$ mm, or, from their median values, $\frac{\sigma_{pre}-\sigma_{post}}{\sigma_{pre}} = 13.9\%$.

We present distributions of the RMSE values calculated per frame for each subset in the form of histograms in Fig. 2b, including their difference.

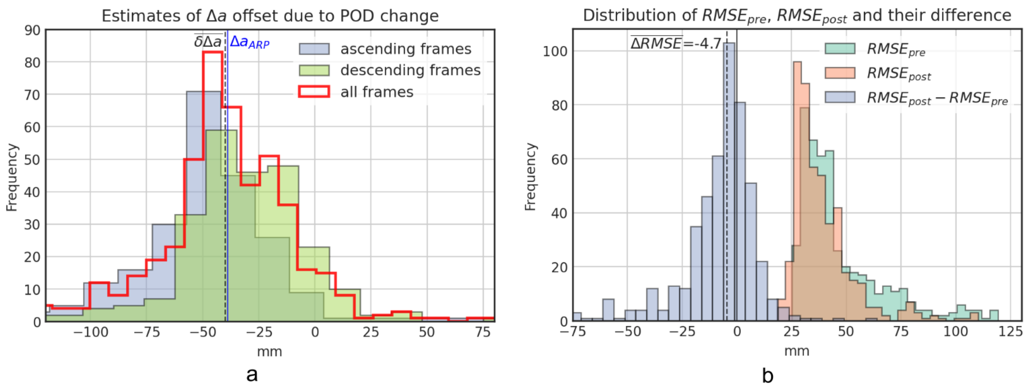

Figure 2. Effect of updated orbits: a) histograms of median difference between Δa values before and after the orbits update. The overall mean value of $\overline{\delta\Delta a} = -39.9 \pm 3.7$ mm agrees, within error, with the given offset of -39 mm for the antenna reference position (Fernández et al., 2019); b) histograms of root mean square errors (RMSE) estimated from equal-size distributions of Δa values from epochs before (*pre*) and after (*post*) the updated orbits, and their difference $\Delta RMSE$, with the median $\overline{\Delta RMSE} = -4.7$ mm.

5 Estimation of plate motion

For the final velocity estimation, we assume that the offset due to the change in orbit products is $\Delta a_{ARP} = 39$ mm, rather than estimate it, as our analysis in the previous section imples this number is accurate.We decompose the velocities into horizontal displacements and compare to values from the ITRF2014 plate motion model.

5.1 Estimation of velocity from Δa

We invert the corrected dataset of Δa values by the linear regression with Huber loss function (Huber, 2009), applied with parameters alpha=1.0 and epsilon=1.35, per frame. We calculate the mean square error, $\sigma^2_{\Delta a}$, assuming two degrees of freedom. We use the mean square error as an estimate of the variance for individual measurements and then apply Eq. 9 to propagate the errors,

$$Q_m = [A^T Q_d^{-1} A]^{-1}, \tag{9}$$

where Q_m is the variance-covariance matrix of the model parameters, $Q_d = \sigma^2_{\Delta a} I_N$ is the NxN variance-covariance matrix of the measurements (I_N being the NxN identity matrix), and $A = [t_i, .., t_N; 1, .., 1]^T$ is an Nx2 matrix where t is the acquisition time in years. The first element of Q_m is the estimate of the variance of velocity σ^2_v. Estimates of velocities in ascending and descending tracks are plotted in Fig. 3.

5.2 Decomposition to N, E directions

We decompose the final Δa-based estimates of horizontal displacement velocity v in the satellite azimuth direction from descending and ascending tracks, to eastwards and northwards direction components, v_E and v_N, respectively. We establish a global grid with a pixel size of approx. 250x250 km, map overlapping frames having their centroid inside the common grid cell, and calculate $\vec{v}_{EN} = [v_E, v_N]^T$ for pixels with $\vec{v} = [v_{D,1}..v_{D,i}..v_{A,1}..v_{A,j}]^T$ ($i > 0, j > 0$ being numbers of overlapping frames from descending and ascending tracks, respectively) by a least squares inversion of

$$\vec{v} = A\,\vec{v}_{EN}, \tag{10}$$

where matrix A contains look vector transformation coefficients per each of $n = i+j$ grouped frames as $A = [\sin\alpha_1..\sin\alpha_n, \cos\alpha_1..\cos\alpha_n]^T$. We estimate the precision of the estimates using propagation of errors as before.

As the azimuth direction contains only a small component of eastwards motion, the eastwards velocity estimates are very sensitive to outliers. We therefore filter our dataset of velocity estimates, removing 66 grid cells that have unreasonably large eastwards velocities or standard deviations: $|v_E| > 200$ mm/year or $\sigma_{v,E} > 50$ mm/year.

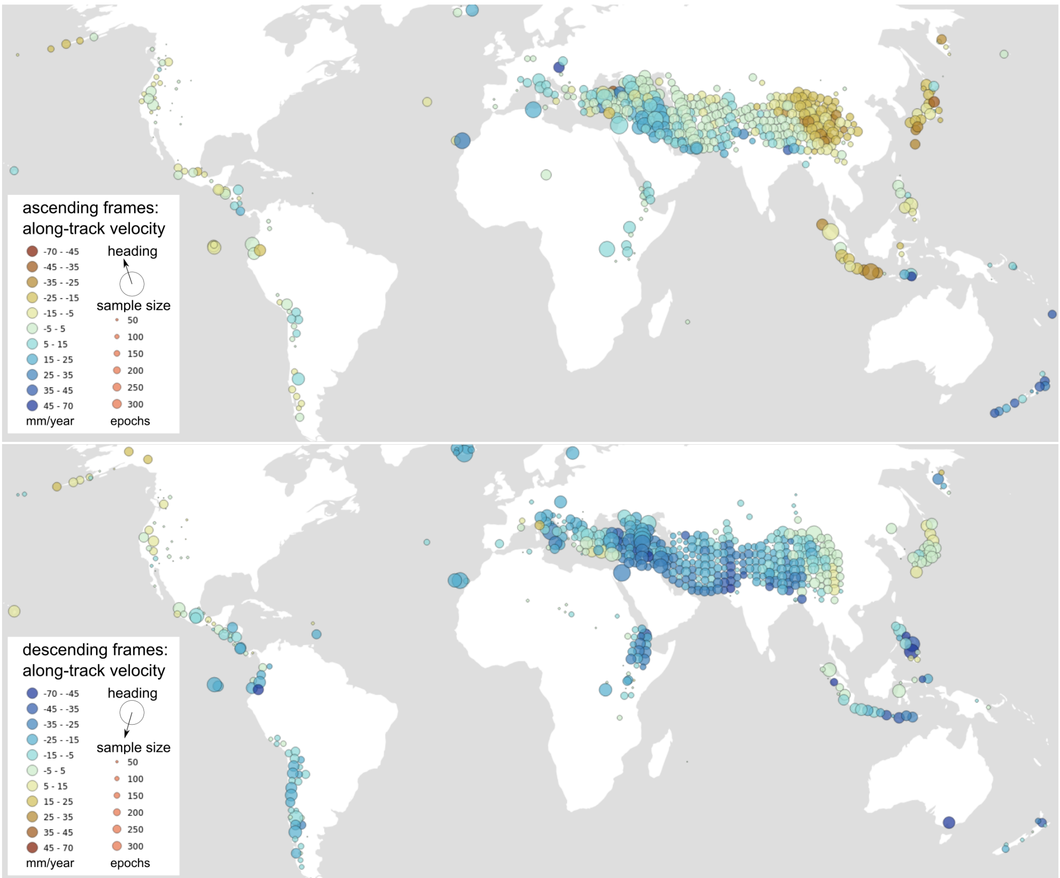

Figure 3. Global overview of along-track motion estimates extracted from ascending (top) and descending (bottom) tracks, after correction for both solid-earth tides and ionosphere. Projection: Robinson, EPSG: 54030.

5.3 Comparison to ITRF2014 plate motion model and summary

We investigate accuracy of the estimates by comparison with the ITRF2014 plate motion model (Altamimi et al., 2017) velocities $\vec{v}_{PMM} = [v_{E,PMM}, v_{N,PMM}]^T$ in both eastwards and northwards directions, averaged per set of coordinates within each of the grid cells. We carry out a statistic evaluation of the quality of our estimates, noting that it will be biased by real differences between the two datasets in plate boundary zones. Median values of v and σ_v for both our full dataset (253 grid cells) and the AHB subset (188 grid cells) are given in Table 1. The ionospheric correction (affecting mainly ascending frames) induced an overall increase of velocity estimates in the eastward component v_E, and in case of AHB subset, it increased also $\sigma_{v,E}$. However, the main component of interest, the northwards velocity v_N, is closer to the values expected by the plate motion model. The table reports average 2-sigma precision over AHB region 3.6 mm/year northwards and 20 mm/year eastwards.

Additionally, we convert the plate motion model velocities to the azimuth direction of each frame as in Eq. 4 and use them to assess accuracy of the original velocity estimates, per direction of orbital tracks (ascending or descending). Their median values are provided in Table 1 as $\overline{v_{PMM}}$.

We visualize the constructed decomposition grid and inverted horizontal velocities by both plate motion model and the final Δa-based estimates after both solid-earth tide and ionosphere corrections in Fig. 4. The figure highlights spatial patterns of a higher deviation from the model that are expected, *e.g.* an increased westward motion of western Turkey (Weiss et al., 2020), but also higher eastwards velocity of the eastern part of the Alpine-Himalayan belt, with respect to the plate motion model.

Fig. 4 also provides a visual comparison of motion vectors from the plate motion model and decomposed Δa-based velocities with and without ionosphere correction, over the AHB region. Including the ionosphere correction gives a generally better fit to the plate motion model in terms of the motion direction, but often leads to an overestimate of velocity magnitude. This is demonstrated quantitatively in Table 1 by the median differences between vector directions and magnitudes before and after ionosphere correction.

Table 1. Median values of estimated velocities v, v_E, v_N [mm/year] and their RMSE (σ) [mm/year] demonstrating impact of solid-earth tides plus ionospheric corrections, and median deviations of vector angle γ and magnitude l of v_E, v_N from the ITRF2014 plate motion model values, in both global dataset and the AHB subset. The subscript tc refers to tide-corrected and tic to tide- and ionosphere-corrected.

global dataset

direction	$\overline{v_{PMM}}$	$\overline{v} \pm \overline{\sigma_v}$	$\overline{v_{tc}} \pm \overline{\sigma_{v,tc}}$	$\overline{v_{tic}} \pm \overline{\sigma_{v,tic}}$
ascending track	0.0	3.2 ± 4.1	3.2 ± 4.0	1.4 ± 3.9
descending track	-7.5	-10.4 ± 3.6	-10.1 ± 3.5	-10.2 ± 3.5
eastwards	28.2	20.1 ± 13.5	22.1 ± 11.3	36.4 ± 11.4
northwards	5.7	9.9 ± 2.6	9.2 ± 2.2	7.4 ± 2.1

Alpine-Himalayan belt subset

direction	$\overline{v_{PMM}}$	$\overline{v} \pm \overline{\sigma_v}$	$\overline{v_{tc}} \pm \overline{\sigma_{v,tc}}$	$\overline{v_{tic}} \pm \overline{\sigma_{v,tic}}$
ascending track	0.7	7.4 ± 2.8	6.7 ± 2.7	2.3 ± 2.7
descending track	-11.0	-15.8 ± 2.5	-15.6 ± 2.4	-15.2 ± 2.4
eastwards	28.5	20.6 ± 12.1	25.9 ± 10.2	41.0 ± 10.0
northwards	6.3	11.9 ± 2.2	12.1 ± 1.8	8.5 ± 1.8

median deviations from the ITRF2014 plate motion model

dataset	$\overline{\Delta\gamma_{tc}}$	$\overline{\Delta\gamma_{tic,PMM}}$	$\overline{\Delta l_{tc,PMM}}$	$\overline{\Delta l_{tic,PMM}}$
global	6.7 deg	0.9 deg	1.8 mm/year	11.5 mm/year
AHB	8.5 deg	1.2 deg	-1.2 mm/year	11.5 mm/year

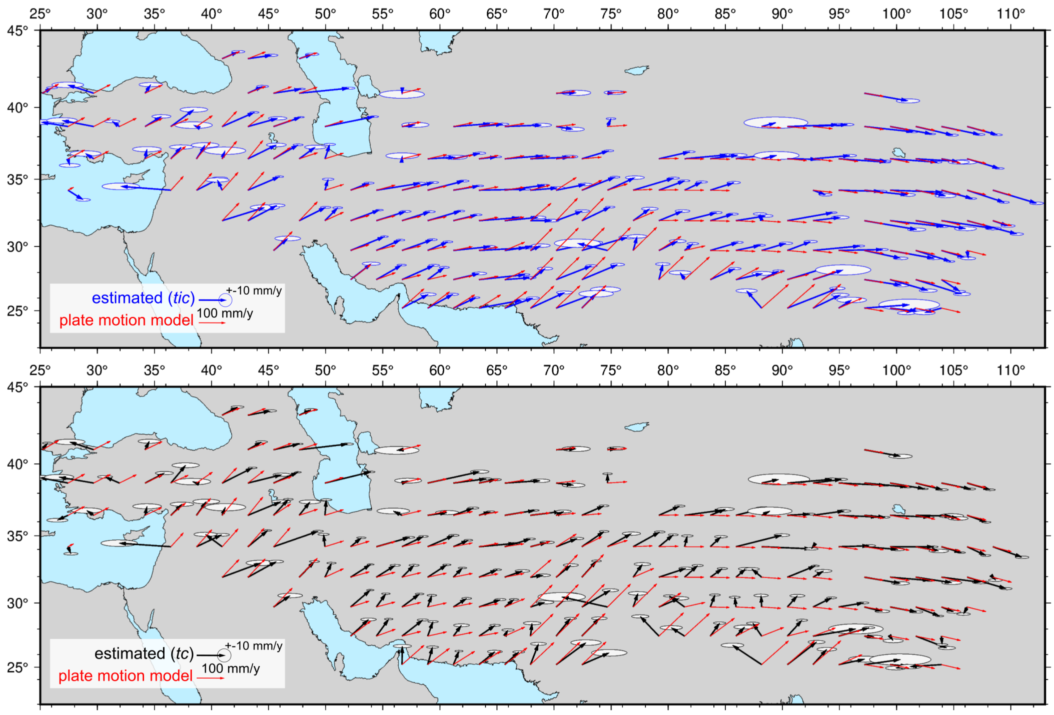

Figure 4. Comparison of estimated velocity vectors to the ITRF2014 plate motion model for the Alpine-Himalayan belt subset, corrected for solid-earth tides and ionosphere (top) and for solid-earth tides only (bottom). Error ellipses represent 1-σ (RMSE) in respective directions, neglecting their possible correlation.

6 Discussion

The list of factors influencing Δa is not comprehensive. For example we do not estimate Δa due to N-S gradients of large scale tropospheric bodies as monsoons, although it technically is possible to model using *e.g.* GACOS service (Yu et al., 2018). Also, we do not incorporate ocean tidal loading that affects some inland areas significantly (Martens et al., 2019). It is our intention to further elaborate on those terms. We will also improve ionospheric correction by performing estimation per swath rather than using single average parameters frame-wise.

We observe large ionospheric signal in Δa values at the end of the Solar Cycle 24 peak, which are not fully corrected, which is most apparent for ascending (dusk) frames before 2017 in Fig. 1. We expect similar effects in the upcoming years due to the next solar cycle (Pesnell, W. Dean, 2020).

Our observations show an overall along-track motion trend for descending frames, of a higher velocity than expected by the ITRF2014 plate motion model. While northwards motion estimates provide a relatively good fit to the values predicted by the plate motion model, the eastwards component has a large bias. This is especially true after ionospheric correction, which increases the estimated eastward velocity component over most of the Alpine-Himalayan belt region by median of 12.5 mm/year. We admit this bias could be induced by our processing approach and should be further investigated.

The coregistration procedure aims to provide Δa estimates in the precision of up to 7 mm (0.0005 pixels). Due to the cascade strategy of using a frame epoch close in time to estimate spectral diversity, previously resampled to the reference epoch, often with support by data from another such epoch, coregistration errors will propagate in time. We did not implement an approach to reduce the error propagation as in (Fattahi, Agram, & Simons, 2017).

Our investigation on the updated orbits in version 1.7 confirms that we can use the reported 39 mm along-track offset of the GPS antenna reference point directly, to perform correction of Δa values after the update of orbits since 2020-07-30, and thus increase the number of data samples, for better estimation of the along-track velocity. Evaluation of the offset in slant range should be also possible, considering the satellite geometry and distance between central points of the GPS and SAR antennas.

7 Conclusions

We demonstrate the possibility of recovering precise measurements of large-scale horizontal motion using azimuth shifts estimated from Sentinel-1 data, using average values in 250x250 km cells. The precision significantly improves after incorporating corrections for solid-earth tides and ionospheric propagation, especially at lower latitudes. However, our corrections only remove a part of the non-deformation component of Δa values, partly due to imperfections of the models we use, and the large averaging over input parameters. Indeed, an updated approach per frame swath could significantly improve the ionospheric correction and will be investigated in future work, or in the final version of this article.

The Δa estimations can be considered along-track measurements that are attached to the global Earth-centered Earth-fixed no-net-rotation framework by GPS-based positioning of Sentinel-1 satellites. Our Δa-based velocity estimates have average 2-sigma precision of around 4 mm/year northwards and 20 mm/year eastwards (see Table 1). They fit reasonably well with the ITRF2014 plate motion model, although there are discrepancies, some of which are expected at plate boundary deformation zones, and some of which are not; there is shift towards the east over the subset of the Alpine-Himalayan belt, on the other hand our estimates correctly identifies a westward motion of Anatolia that is not included in the model.

We investigate and incorporate corrections due to new orbit ephemerides products, which shift Δa values after 2020-07-30 by -39 mm, allowing for a seamless combination of all available Δa values for precise velocity estimates. We estimate the offset as -39.9 ± 3.7 mm at 2-sigma error. We also observe an increased precision of Δa using the updated orbits, improved by 13.9% or by 4.7 mm in RMSE.

Further research should analyse across-track (range) measurements in combination to the along-track InSAR approach, and include use of other models to decrease along-track residuals - primarily a polar motion and ocean loading tide model, as well as ECMWF-derived tropospheric delays, for example by COMET GACOS products (Yu et al., 2018). Finally, the new Sentinel-1 external products known as S1_ETAD (Gisinger et al., 2021) should provide valuable correction data for Sentinel-1 bursts, including ionospheric, solid-earth tide, ocean tide load and other corrections.

We provide data used within this article as an indexed supplementary material, however we also aim to share the original Δa and Δr values within the community in a systematic manner, as an additional new open product of the COMET LiCSAR system.

Acknowledgments

This work is supported by The Natural Environment Research Council large grant, “Looking inside the continents from Space” (NE/K010867/1). COMET is the NERC Centre for the Observation and Modelling of Earthquakes, Volcanoes and Tectonics, a partnership between UK Universities and the British Geological Survey. This work contains modified Copernicus Sentinel-1 data [2014-2021] analysed by COMET LiCSAR system at JASMIN,

the UK's collaborative data analysis environment (`https://jasmin.ac.uk`), and ARC4, part of the High Performance Computing facilities at the University of Leeds, UK. We used available open-source models to perform corrections on solid-earth tides and ionosphere, and ITRF2014 plate motion model values extracted from UNAVCO website.

The output datasets described here, including an interactive KMZ layer (Google Earth) of Δa time series plots per frame, are available under Creative Commons 4.0 license from DOI:????/zenodo.???? (will be included during final submission). The processing code is available under GNU GPL 3.0 license from `https://gitlab.com/comet_licsar/daz`.

The authors wish to thank Dr. Heike Peter, Dr. Pawan Piromthong, Dr. Chris Rollins and Dr. Jonathan Weiss for helpful discussions.

References

Altamimi, Z., Métivier, L., Rebischung, P., Rouby, H., & Collilieux, X. (2017, 03). ITRF2014 plate motion model. *Geophysical Journal International*, *209*(3), 1906-1912. Retrieved from `https://doi.org/10.1093/gji/ggx136` doi: 10.1093/gji/ggx136

Bechor, N. B. D., & Zebker, H. A. (2006). Measuring two-dimensional movements using a single insar pair. *Geophysical Research Letters*, *33*(16). Retrieved from `https://agupubs.onlinelibrary.wiley.com/doi/abs/10.1029/2006GL026883` doi: https://doi.org/10.1029/2006GL026883

Bilitza, D., Altadill, D., Truhlik, V., Shubin, V., Galkin, I., Reinisch, B., & Huang, X. (2017). International reference ionosphere 2016: From ionospheric climate to real-time weather predictions. *Space Weather*, *15*(2), 418-429. Retrieved from `https://agupubs.onlinelibrary.wiley.com/doi/abs/10.1002/2016SW001593` doi: https://doi.org/10.1002/2016SW001593

De Zan, F., & Monti Guarnieri, A. (2006). Topsar: Terrain observation by progressive scans. *IEEE Transactions on Geoscience and Remote Sensing*, *44*(9), 2352-2360. doi: 10.1109/TGRS.2006.873853

Ducarme, B., & Schüller, K. (2018). Canonical wave grouping as the key to optimal tidal analysis. *Bulletin d'Informations Marees Terrestres (BIM)*, *150*, 12131–12244.

Fattahi, H., Agram, P., & Simons, M. (2017). A network-based enhanced spectral diversity approach for tops time-series analysis. *IEEE Transactions on Geoscience and Remote Sensing*, *55*(2), 777-786. doi: 10.1109/TGRS.2016.2614925

Fattahi, H., Simons, M., & Agram, P. (2017). Insar time-series estimation of the ionospheric phase delay: An extension of the split range-spectrum technique. *IEEE Transactions on Geoscience and Remote Sensing*, *55*(10), 5984-5996. doi: 10.1109/TGRS.2017.2718566

Fernández, M., Aguilar, J. A., & Fernández, J. (2019). *Sentinel-1 properties for gps pod: Copernicus sentinel-1, -2, and -3 precise orbit determination service (sentinelspod).* Retrieved from `https://sentinels.copernicus.eu/documents/247904/3455957/Sentinel-1-properties-for-GPS-POD`

Gisinger, C., Schubert, A., Breit, H., Garthwaite, M., Balss, U., Willberg, M., ... Miranda, N. (2021). In-depth verification of sentinel-1 and terrasar-x geolocation accuracy using the australian corner reflector array. *IEEE Transactions on Geoscience and Remote Sensing*, *59*(2), 1154-1181. doi: 10.1109/TGRS.2019.2961248

Gomba, G., Parizzi, A., De Zan, F., Eineder, M., & Bamler, R. (2016). Toward operational compensation of ionospheric effects in sar interferograms: The split-spectrum method. *IEEE Transactions on Geoscience and Remote Sensing*, *54*(3), 1446-1461. doi: 10.1109/TGRS.2015.2481079

Grandin, R., Klein, E., Métois, M., & Vigny, C. (2016). Three-dimensional displacement field of the 2015 mw8.3 illapel earthquake (chile) from across- and along-track sentinel-1 tops interferometry. *Geophysical Research Letters*, *43*(6), 2552-2561. Retrieved from `https://agupubs.onlinelibrary.wiley.com/doi/abs/10.1002/2016GL067954` doi: https://doi.org/10.1002/2016GL067954

Hooper, A. J., Piromthong, P., Elliott, J. R., Weiss, J. R., & Lazecky, M. (2020, December). The improvement to high-resolution maps of interseismic strain accumulation from incorporating Sentinel-1 along-track measurements. In *Agu fall meeting abstracts* (Vol. 2020, p. G018-07).

Hoque, M., & Jakowski, N. (2012, 02). Ionospheric propagation effects on gnss signals and new correction approaches.. doi: 10.5772/30090

Huber, P. (2009). *Robust statistics*. Hoboken, N.J: Wiley.

Lazecký, M., Spaans, K., González, P. J., Maghsoudi, Y., Morishita, Y., Albino, F., ... Wright, T. J. (2020). Licsar: An automatic insar tool for measuring and monitoring tectonic and volcanic activity. *Remote Sensing*, *12*(15). Retrieved from `https://www.mdpi.com/2072-4292/12/15/2430` doi: 10.3390/rs12152430

Li, X., Jónsson, S., & Cao, Y. (2021). Interseismic deformation from sentinel-1 burst-overlap interferometry: Application to the southern dead sea fault. *Earth and Space Science Open Archive*, 13. Retrieved from `https://doi.org/10.1002/essoar.10506585.1` doi: 10.1002/essoar.10506585.1

Liang, C., Agram, P., Simons, M., & Fielding, E. J. (2019). Ionospheric correction of insar time series analysis of c-band sentinel-1 tops data. *IEEE Transactions on Geoscience and Remote Sensing*, *57*(9), 6755-6773. doi: 10.1109/TGRS.2019.2908494

Martens, H. R., Rivera, L., & Simons, M. (2019). Loaddef: A python-based toolkit to model elastic deformation caused by surface mass loading on spherically symmetric bodies. *Earth and Space Science*, *6*(2), 311-323. Retrieved from `https://agupubs.onlinelibrary.wiley.com/doi/abs/10.1029/2018EA000462` doi: https://doi.org/10.1029/2018EA000462

Pesnell, W. Dean. (2020). Lessons learned from predictions of solar cycle 24. *J. Space Weather Space Clim.*, *10*, 60. Retrieved from `https://doi.org/10.1051/swsc/2020060` doi: 10.1051/swsc/2020060

Peter, H., Fernández, J., & Féménias, P. (2020). Copernicus sentinel-1 satellites: sensitivity of antenna offset estimation to orbit and observation modelling. *Advances in Geosciences*, *50*, 87–100. Retrieved from `https://adgeo.copernicus.org/articles/50/87/2020/` doi: 10.5194/adgeo-50-87-2020

Peter, H., Fernández, M., Arnold, D., Duan, B., Simons, W., Gini, F., ... Féménias, P. (2021, April). Copernicus POD Service - Orbit reprocessing for Copernicus Sentinel-1 satellites. In *Egu general assembly conference abstracts* (p. EGU21-5296).

Peter, H., Usón, M. F., Aguilar, J. A., & Fernández, J. (2021). *Copernicus pod product handbook: Copernicus sentinel-1, -2 and -3 precise orbit determination service (cpod)*. Retrieved from `https://sentinels.copernicus.eu/documents/247904/3372484/Sentinels-POD-Product-Handbook-1.19.pdf`

Petit, G., & Luzum, B. (2013). The 2010 reference edition of the iers conventions. In Z. Altamimi & X. Collilieux (Eds.), *Reference frames for applications in geosciences* (pp. 57–61). Berlin, Heidelberg: Springer Berlin Heidelberg.

Weiss, J. R., Walters, R. J., Morishita, Y., Wright, T. J., Lazecky, M., Wang, H., ... Parsons, B. (2020). High-resolution surface velocities and strain for anatolia from sentinel-1 insar and gnss data. *Geophysical Research Letters*, *47*(17), e2020GL087376. Retrieved from `https://agupubs.onlinelibrary.wiley.com/doi/abs/10.1029/2020GL087376` (e2020GL087376 2020GL087376) doi: https://doi.org/10.1029/2020GL087376

Ya'acob, N., Abdullah, M., & Ismail, M. (2010, 03). Gps total electron content (tec) prediction at ionosphere layer over the equatorial region.. doi: 10.5772/8474

Yagüe-Martínez, N., Prats-Iraola, P., Rodríguez González, F., Brcic, R., Shau, R., Geudtner, D., ... Bamler, R. (2016). Interferometric processing of sentinel-1 tops data. *IEEE Transactions on Geoscience and Remote Sensing*, *54*(4), 2220-2234. doi: 10.1109/TGRS.2015.2497902

Yu, C., Li, Z., Penna, N. T., & Crippa, P. (2018). Generic atmospheric correction model for interferometric synthetic aperture radar observations. *Journal of Geophysical Research: Solid Earth*, *123*(10), 9202-9222. Retrieved from `https://agupubs`

.onlinelibrary.wiley.com/doi/abs/10.1029/2017JB015305 doi: https://doi.org/10.1029/2017JB015305